Master's Thesis of Landscape Architecture

Analyzing the Difference in Vegetation Index of Urban Forest Edge by Land Cover Types using Spatio-temporal Fusion Image

인접 토지피복에 따른 도시 산림 임연부의 식생지수 차이 분석 - 시공간 융합 기법 영상을 활용하여 -

February 2019

Graduate School of Seoul National University
Department of Landscape Architecture and Rural Systems Engineering, Landscape Architecture Major

Woong Gi Sung

Analyzing the Difference in Vegetation Index of Urban Forest Edge by Land Cover Types using Spatio-temporal Fusion Image

Under the Direction of Adviser, Prof. Dong Kun Lee

Submitting a master's thesis of
Landscape Architecture

October, 2018

Graduate School of
Seoul National University
Department of Landscape Architecture and Rural Systems Engineering, Landscape Architecture Major

Woong Gi Sung

Confirming the master's thesis written by
Woong Gi Sung

December, 2018

Chair _____(Seal)

Vice Chair _____(Seal)

Examiner _____(Seal)

Abstract

Due to urbanization and human impacts, the forests in the urban areas have been getting fragmented and forest edges are increasing. Since forest edges have a larger exposure than the forest interiors, they are more exposed by heat from neighbored buildings and especially adjacent land cover types result in low soil moisture and vegetation condition. Forest edge monitoring requires high spatio-temporal resolution. Landsat and MODIS images, which are available for free nor difficult to use, have limitations on temporal resolution and spatial resolution, respectively. Therefore, in this paper, we used RDSFM (Residual Distribution based Spatiotemporal Data Fusion Method) data fusion method to make continuous NDVI images with high temporal and spatial resolution using Landsat and MODIS images. Then we derived $NDVI_{max}$ image with continuous NDVI images to evaluate vegetation conditions between the urban forest edges by different land cover types. We analyzed the differences of vegetation condition and the distance that the forest edges are affected due to adjacent land cover types (Residence, Road, Agriculture, Grassland) using $NDVI_{max}$ image. We found that both

$NDVI_{max}$ values of the broad leaf and the needle leaf forest 30m edge was the lowest, and higher values was derived as the distance increased from the forest edge to forest interior. In other words, the edges of both forest types were affected by the adjacent land cover types. The type of land cover, which had the greatest effect on the forest edge was shown as road, and the effect range was found to be up to 90 meters from the forest edge. This means the management of the forest edge nearby roads will be necessary during road development and also after development. The $NDVI_{max}$ values of forest edge neighbored by agricultural area, were higher than the $NDVI_{max}$ values of forest edge neighbored by developed areas such as residential areas and roads. This means agricultural area could be used as a buffer for preserving vegetation from developed area. In the case of grassland, $NDVI_{max}$ value was higher than that of the forest edge neighbored by the road, but lower than residential area and agricultural area. The low $NDVI_{max}$ value of forest edge near grassland seems to be due to artificially made grassland. Artificial grassland includes which were cut-off surface and construction area before it were created to be grassland. This study is meaningful for evaluating vegetation condition by

different land cover types and vegetation condition difference from the edge to forest interior by 30m distance to 90m based on $NDVI_{max}$ image derived by RDSFM. The results of this study are expected to be useful for assessing the effects of land cover types and land cover change on adjacent forest edges in terms of urban forest monitoring and management of urban forests.

Keyword : Urban forest, Forest edge, Land cover type, Data Fusion, Normalized Difference Vegetation Index (NDVI)

Student Number : 2017-20179

Table of Contents

List of Figures

List of Tables

Chapter 1. Introduction

Urban forests provide diverse services to urban ecosystems, as well as social and economic benefits of recreation and tourism (Gobster & Westphal 2004). In particular, urban forests play a role in carbon pools that absorb atmospheric carbon dioxide (Magnago et al. 2014), improving air quality (Escobedo et al. 2009), reducing greenhouse gases (Lal 2005), thermal comfort (Shahidan et al. 2010), minimizing the energy use by providing building shade (Akamphon 2014), and microclimate control. It is also an important element of the urban ecosystem which benefits to protection of biodiversity, prevention of soil erosions, facilitation of nutrient circulation, prevention of floods and reduction of heat island impacts (Shojanoori & Shafri 2016; Akamphon 2014).

Urbanization and increase of human activities changed not only land cover types but also urban forests. The forests in urban areas have been getting fragmented and forest edges are increasing (Miller 2012). Since forests edges have different characteristics of light availability, air circulation, nutrients, air

temperature, and humidity than interior forest (Hofmeister et al. 2013). The increase of forest edges would facilitate invasions of exotic species and reduce habitat quality, species composition, diversity, forest productivity, carbon stocks and carbon absorption capacity (Briber et al. 2015; Kim et al. 2016; Xun et al. 2014).

Urban forests are more exposed than natural forests and are more likely to be affected by winds generated by buildings, high light intensity by direct sun light, adjacent buildings and paved surfaces (Kuttler 2008; Sung & Park 2000). In addition, the characteristics of the forest would be different from the edge to interior and also due to temporal change. Therefore, in terms of urban forest management, it is necessary to understand more clearly about the role of urban forests by monitoring the influence of adjacent land cover on the forests edges through analyzing the vegetation condition.

Previous studies have shown that the urban forest edges were affected by adjacent land cover types, and as they had more artificiality, more exotic species were observed (Lososova et al. 2012). Song (2005) compared and analyzed the ratio of exotic

species in forests for each land cover type. Higher ratio of exotic species was derived in the order of railroad, industrial area, residential area, and forest. In other words, it was revealed that the influence degrees were different according to the type of land use. However, studies of estimating the influence of adjacent land cover types and the extent of distance from land cover types to forest edges are very limited.

There were several studies based on field surveys in the forest edges which were adjacent to pasture area (Davies Colley et al. 2000), cultivated lands (Hernandez-Santana et al. 2011), deforested area (Baker et al.2014) and fragmented rainforests in tropical area (Magnago et al. 2011). In Korea, analyzing the difference of carbon stocks between forests and forest edges based on field surveys (Sung et al. 2015) was conducted. Sung et al. (2015) used the allometric equation and the carbon conversion factors. This study derived that as an individual species, the carbon stocks of the interior forest were higher. However, field-based research has limitations such as limited spatial extent, time intensive, and high cost (MacLean 2017).

Satellite images provide a wide range of information of areas periodically and make the analysis more objective. Many studies have been conducted vegetation evaluation using various indices based on satellite images. Hansen et al. (2013) assessed global forest loss using Landsat images. Sebastian & Howard (2005) compared Landsat 7 Normalized Difference Vegetation Index (NDVI) images and Leaf Area Index (LAI) to evaluate the vegetation community structure and ecosystem characteristics of forest edges. The NDVI value derived from the satellite image is one of vegetation indices that indirectly representing the vegetation condition of the surface, which is closely related to the biomass and photosynthesis of the vegetation (Baldi et al. 2008). Variations of NDVI values reflect the changes in vegetation so that NDVI is widely used in vegetation related studies.

Urban forest edge monitoring requires high spatio-temporal resolution images for continuous monitoring (Li et al. 2017). Among the satellite data currently available, the most accessible and provided for free are Landsat and MODIS images. Landsat images have 30m spatial resolution with 16 day temporal

resolution. However, it is difficult to acquire continuous data due to the influence of cloud and unstable atmosphere in Korea, especially on June to August.

To complement temporal resolution, which is a limitation of Landsat image, there were several image fusion studies using MODIS images provided by United States Geological Survey (USGS) (Zhu et al. 2010; Wu et al. 2015, 2016). Spatial and temporal adaptive reflectance fusion model (STARFM) is one of the representative fusion technique, but it has low accuracy on predicting the image in complex areas such as cities (Liu et al. 2012; Weng et al. 2014). One of the recently developed image fusion technique is Flexible Spatiotemporal DATA Fusion (FSDAF). It requires only one period of clear images, which need less input data than other image fusion techniques.

FSDAF is an image fusion technique that have high accuracy even in heterogeneous areas, such as cities (Zhu et al. 2016). However, it has relatively low prediction accuracy in the NIR band which is used for vegetation survey. Residual Distribution based Spatio-temporal Data Fusion Method (RDSFM) were developed to improve the prediction accuracy of each band,

especially NIR band which were the limitation of FSDAF (Jin 2018).

Therefore, in this study, we tried to analyze the differences of vegetation condition and the distance that the forest edges are affected according to adjacent land cover types using the NDVI images which were derived by RDSFM. The results of this study can be used as the base data of vegetation monitoring and forest management. In addition, this study is expected to provide base data on areas that need priority management and the range of the management that is required for each type of adjacent land cover.

Chapter 2. Literature Review

2.1. Spatio-temporal data fusion methods

Temporal resolution and spatial resolution of satellite images play an important role in vegetation monitoring and vegetation related studies. Especially, time series data is important for vegetation monitoring (Shun et al. 2011), evaluation of drought impact on vegetation (Gouveia et al. 2017), vegetation degradation (Zhou et al. 2013). In areas where land cover is heterogeneous, images with high spatial resolution as well as high temporal resolution are required. Therefore, recently, spatio-temporal image fusion techniques have been developed to produce images with improved spatial and temporal resolution (Zhu et al. 2010; Wu et al. 2015).

Spatio-temporal image fusion techniques include weighted function-based, unmixing-based, and dictionary-pair learning methods. In this study, we reviewed each image fusion technique.

2.1.1. Weighted function based fusion method

In weighted-function-based method, neighboring pixels which have similar values are selected in order to predict a target pixel value in the moving window. Then, the weights which are based on distance between the pixels and the target pixel, spectral difference between the sensors, temporal changes are calculated considering contribution to predict target pixel.

Among the weighted-function-based method, the Spatial and Temporal Adaptive Reflectance Fusion Model (STARFM) is the one that were developed first by Gao et al. (2006), requires at least one pair of coarse image and fine image at t_1, and coarse image of predict time t_2. STARFM predicts the fine image by combining weights on the target pixel. The fine image is used to select a similar pixel for predicting the target pixel, and it is selected through the standard deviation with the target pixel within the same land cover type. STARFM detects the reflectance value through similar neighboring pixels that are weighted by spectral, temporal, and spatial distances. However, the STARFM have a low of accuracy where land cover types are

mixed in a single coarse pixel (Gao et al. 2006; Cammalleri et al. 2014). Therefore, to overcome the limitation of STARFM, Spatial Temporal Adaptive Algorithm for mapping Reflectance Change (STAARCH) (Hilker et al. 2009) which reflects land cover change better and Enhanced Spatial and Temporal Adaptive Reflectance Fusion Model (ESTARFM) (Zhu et al. 2010) which has improved accuracy in heterogeneous landscapes have been developed.

2.1.2. Unmixing based fusion method

One of the unmixing-based methods, Multi Sensor Multiresolution Technique (MMT) was proposed by Zhukov et al. (1999), as the first one which acquired fused image at different times with different resolutions. MMT first classifies the fine image to define endmembers at coarse image. Then calculate the endmember fractions of each coarse pixel and unmixes the coarse pixel at the prediction date within the moving window. Finally, assigns unmixed reflectance values to fine pixels (Zhukov et al. 1999). Several studies have modified MMT to improve the accuracy of the fused results (Gevaert & García-Haro 2015; Zhu et al. 2016).

Flexible Spatiotemporal DAta Fusion (FSDAF) is another image fusion technique that is based on unmixing-based method proposed by Zhu et al. (2016). The FSDAF requires minimal input data but has higher accuracy on predicting images in heterogeneous areas than weighted-based method. However, FSDAF cannot capture the change of reflectance values within a range in each band because it provides same weights to bands in target pixel. It causes errors especially where the landscape changes or has different seasonal change such as vegetation area.

Recently, Residual Distribution based Spatio-temporal Data Fusion Method (RDSFM) have been developed by Jin (2018) to improve the limitations of FSDAF. As the RDSFM distributes the Multi-variate Alternation Detection (MAD) weight-based residuals to each band, it shows improved prediction accuracy compared to FSDAF. This method can effectively predict where spectrum changes due to land cover or within class-variance (Jin 2018).

2.1.3. Dictionary-pair learning fusion method

Dictionary-pair learning based method establish correspondences between fine and coarse images based on the structural similarity of two images which can be used to capture land cover changes. Sparse-representation-based Spatio Temporal reflectance Fusion Model (SPSTFM) (Huang and Song. 2013) and one-pair learning (Song and Huang. 2013) are one of the dictionary-pair learning based method. SPSTFM shows the correlation between two fine and coarse images, and predicts the fine image of the predicted date using the trained dictionary. The dictionary-based learning method uses only the statistical relationship between the fine and coarse images rather than the physical characteristics of the remote sensing signal. It can predict the change of the land cover better, but if the scale difference between the fine image and the coarse image is large the predict accuracy will be low (Song & Huang 2013).

Table 1. List of image fusion method

Fusion method	Input data	Pros/Cons	Reference
STARFM (Weighted function based)	One or more pairs	Relatively high predict accuracy in homogenous area but low predict accuracy in heterogenous area	Gao et al. (2006)
STAARCH (Weighted function based)	Two fine images and time-series of coarse images	Lots of input data is required	Hiker et al. (2009)
ESTARFM (Weighted function based)	Two pairs	Doesn't reflects rapid land cover change	Zhu et al. (2010)
MMT (Unmixing baesd)	One fine image	Predict accuracy is low and there is a noise within the image that occurs errors	Zhukov et al. (1999)
FSDAF (Unmixing baesd)	One pair	Requires minimal input data, but causes errors especially where the landscape changes or has different seasonal change such as vegetation area	Zhu et al. (2016)
RDSFM (Unmixing baesd)	One pair	RDSFM shows improved prediction accuracy compared to FSDAF where spectrum changes due to land cover or within class-variance	Jin (2018)
SPSTFM (Dictionary-pair learning)	Two pairs	Lots of input data is required	Huang & Song (2012)

One-pair learning (Dictionary-pair learning)	One pair	Predicts well in land cover changed area, but has a low prediction accuracy when scale difference of coarse and fine image is large	Song & Huang (2013)

* Only the required data are listed in the table, as all methods need one coarse image at prediction date as an input.

2.2. Forest edge evaluation method

2.2.1. Forest edge evaluation based on field survey

Various studies have been conducted in forest edges. Davies-Colley et al. (2000) measured wind speed, atmospheric temperature, soil temperature, and vapor pressure in forest edges adjacent to pasture area. They found the variables were stabilized at 40m from the forest edges and suggested 40m as a buffer zone. Magnago et al. (2014) conducted a study on the relationship between the microclimate of forest edges and vegetation structure, and found that microclimate could be regarded as a major factor explaining the differences in forest structure within forest edges. Alignier & Deconchat (2013)

conducted a study about changes of vegetation characteristics of forest edges and the forest patch size through measuring understory vegetation composition, biodiversity, vegetation cover rate, soil temperature and moisture.

In Korea, a study was conducted to analyze the difference in carbon stocks between forest edges and interior based on field surveys (Sung et al. 2015). Sung et al. (2015) used connectivity analysis, separating forest interior and edge. In the forest edge, a large range of various species and shrubs were revealed. In addition, the carbon stocks of forest edge were found to be lower than those in the forest interior.

Kim et al. (2017) investigated the changes of pine forest edges after deforestation in southern part of Gangwon area by comparing the abiotic factors (air temperature, air humidity) and biotic factors (vegetation richness, canopy openness). The direct and indirect effect of deforestation has shown that it has a continuous impact from 15m to 20m from the forest edge. However, field-based studies have limitations such as limited spatial extent, time intensive, and high cost (MacLean 2017).

2.2.2. Forest edge evaluation based on satellite image

Satellite images have lots of advantages, being able to investigate a wide range of area, acquire long-term data. Several advantages of satellite images make it possible to investigate characteristics of seasonal change of forests. Hansen et al. (2013) conducted a study to estimate worldwide forest area, forest loss and increase using Landsat images from 2000 to 2012.

Sebastian & Howard (2005) evaluated the vegetation community structure and characteristics of forest edges by analyzing the Landsat 7 Normalized Difference Vegetation Index (NDVI) images, Leaf Area Index (LAI) and species composition. NDVI and LAI values reduced as they get closer to the forest edge. Jin et al. (2017) evaluated the quantitative and qualitative reduction of annual average Net Primary Production (NPP) in the development area using FSDAF and CASA-NPP model.

The NDVI value derived from the satellite image is an indicator that reflects the presence and status of vegetation. NDVI is one of the most widely used vegetation indices and it is closely

related to functional characteristics of vegetation, productivity of vegetation, photosynthetic activity of the vegetation (Baldi et al. 2008). NDVI variation reflects changes in vegetation, so they are widely used in vegetation related studies. NDVI is a vegetation index based on features of vegetation that has high reflectance in the NIR band and low reflectance in the red band for healthy vegetation (Rouse et al. 1973) (see Equation (1)). The value of NDVI is calculated as −1 to + 1. When the vegetation is in a good condition, this index is close to + 1 and the value decreases in case of vegetation degradation or destruction (Khosravi et al. 2017).

$$NDVI = \frac{(NIR - red)}{(NIR + red)} \quad (1)$$

2.3. Literature review conclusion

Previous studies have been carried out field-based studies in the past, but recently studies that investigate ecological changes of vegetation using satellite images are increasing. Although many studies have been conducted to evaluate the forest edge using satellite image, few studies have addressed differences in vegetation condition due to adjacent land cover, and the distance that each land cover type affects the neighbored forest edges. Urban forest monitoring requires high spatial and temporal resolution for continuous monitoring and its heterogeneous landscape. Therefore, in this study, the NDVI images were obtained by using RDSFM, which has recently been developed and has high prediction accuracy even in heterogeneous areas such as urban areas. We tried to analyze the differences of vegetation condition and the distance that the forest edges are affected due to adjacent land cover types using NDVI images which were derived by RDSFM.

Chapter 3. Materials and Methods

3.1. Study scope

3.1.1. Spatiotemporal scope

In this study, we analyzed the urban forest edges in Seoul Metropolitan area where urbanization and deforestation have been progressed (Figure 1). Seoul is a large city with a total population of about ten million (KOSIS 2015). In the center of Seoul, urbanized area as commercial and residential areas are concentrated around the Han River. The outer part of the city, large scale of urban forest is located and small scale of forest is scattered in the inner part of the city.

The edges of urban forests are defined as 90m, referring to the range of edge effect in previous studies (Riutta et al. 2014; Haddad et al. 2015). To investigate the differences of vegetation condition of the forest edges due to adjacent land cover types and the distance that they are affected, we compared NDVI values that is located in 30m, 60m, 90m from the forest edge.

The temporal scope of the study was set to 2015.

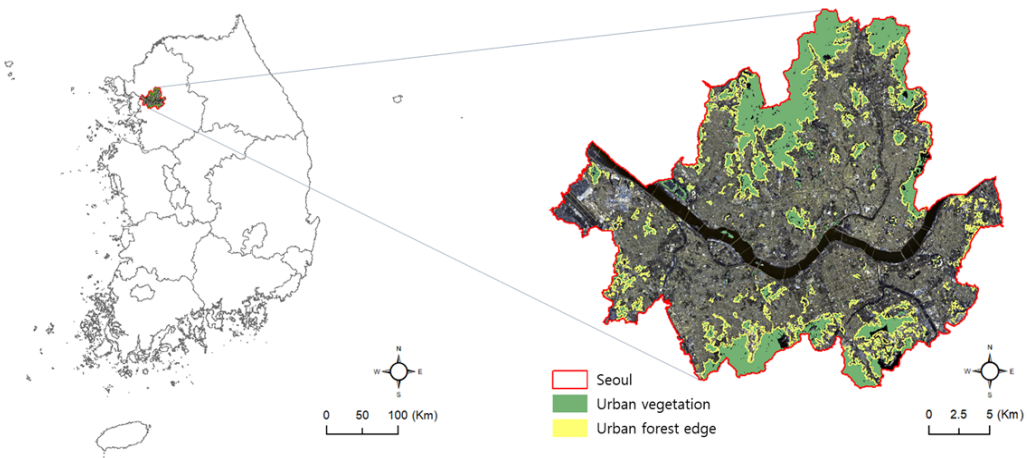

Figure 1. Study site (Sung et al. 2018)

3.1.2. Contextual scope

The contextual scope of this study is to evaluate the difference in vegetation conditions of forest edges according to adjacent land cover types and the difference in vegetation condition according to the distance from the forest edge to the forest interior in Seoul. However, images with high spatial and temporal resolution are required to evaluate differences of vegetation condition of forest edges. Therefore, we used RDSFM to derive continuous NDVI images to evaluate the vegetation condition

differences of the urban forest edges in 2015.

3.2. Research method

3.2.1. Research flow

The research flow of this study is shown in Figure 2. First, Landsat 8 OLI images and MODIS MCD43A4 images of 2015 were collected. After image preprocessing, we constructed a continuous NDVI images of 2015 with 30m spatial resolution using the RDSFM.

Root Mean Square Error (RMSE), Correlation coefficient R, Average Difference (AD) between the predicted image and the actual Landsat image were used for accuracy verification. $NDVI_{max}$ image was derived with verified continuous NDVI images that reflects the maximum vegetation condition of the year.

Lastly, we used land cover map (2013) provided by Environmental Geographic Information Service (EGIS) and the 5^{th} forest type map to analyze the differences of vegetation

condition and the distance that the forest edges are affected due to adjacent land cover types. The ANOVA analysis was conducted to detect the significant differences of $NDVI_{max}$ according to adjacent land cover types and distance of the forest edge using SPSS software.

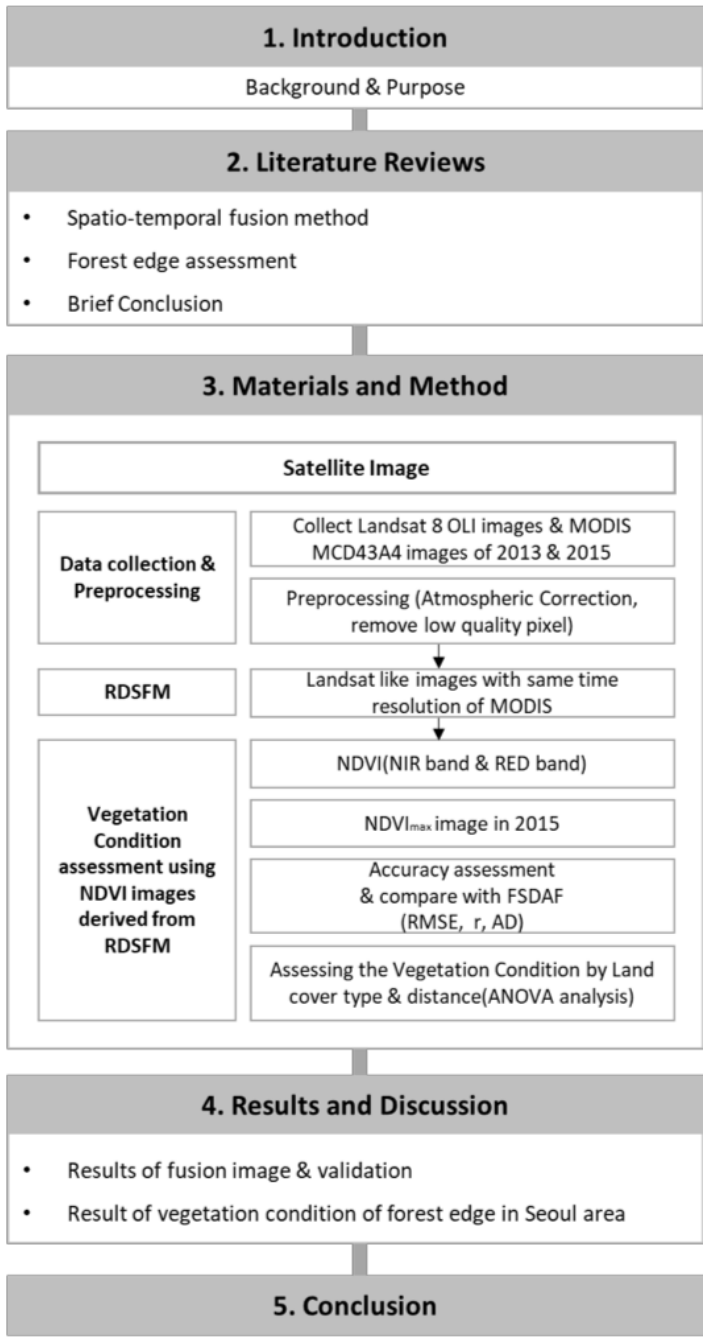

Figure 2. Study flow

3.2.2. Data collection and pre-processing

MODIS images that have low spatial resolution but high temporal resolution and Landsat 8 OLI images that have relatively high spatial resolution but low temporal resolution were used as an input of RDSFM. In order to improve the accuracy of the image prediction, we used the image of September 16th, which had the lowest cloud cover among the Landsat images of 2013. MODIS MCD43A4 Reflectance images were used from January to December to predict Landsat-like image. MCD43A4 images have a spatial resolution of 500m and a temporal resolution of 1 day, and each image is a 16 day composite image. The images that were used for image fusion are presented in Table 2.

All Landsat images used in this study were applied for atmospheric correction using FLAASH in order to minimize the influence of atmosphere and atmospheric refractions (FLAASH 2009). MODIS images were reprojected to UTM 52 zone coordinates as the same as Landsat image, using MODIS Reprojection Tool (MRT) to minimize geometrical distortion

between Landsat image. The spatial resolution of MODIS image was resized to 480m for the image fusion with Landsat image. The quality reliability mask band was used to remove the anomalies of the images.

Table 2. The image data used in this study

Data Type	Acquire Time	Spatial Resolution	Cloud	Band	Role	Tile
Landsat 8 OLI	2013.9.16	30m	0.3%	red, NIR band	Input (fine resolution image at t_1; F_1)	Path 116 Row 34
	2015.3.14		0.5%		Validation	
	2015.9.22		1.4%			
MCD43A4 (500m_daily _Reflectance)	2013.9.16	500m	-	red, NIR, SWIR band	Input (Coarse resolution image at t_1; C_1)	h28 v05
	2015.1.1~ 2015.12.31				Input/Predict (Coarse resolution image at t_2; C_2)	

3.2.3. Image fusion method

In this study, the predicted image derived from RDSFM was tested using a real landscape image and compared with FSDAF. There were lots of cases comparing fused image in other countries such as Australia (Emelyanova et al. 2013), North Korea (Jin 2018). However, there have been few cases comparing fused image in Seoul Metropolitan area. Therefore, in this study, we tried to find out whether it is applicable to Seoul area where the landscape is highly mixed through comparing verification results between predicted images derived from RDSFM and FSDAF.

3.2.3.1. Image fusion using FSDAF method

The FSDAF is based on unmixing-based fusion technique which requires a pair of Landsat image and MODIS image at reference time t_1, MODIS image at prediction time t_2. FSDAF proceeds through the following five steps (Figure 3).

1) Classify the fine resolution image at t_1 using unsupervised

classification

In order to get the fraction of each class within one coarse pixel, the fine resolution image at t_1 is classified by ISO DATA unsupervised classification using all image bands. The fractions of each class within a coarse pixel was calculated through counting the number of fine pixels of each class:

$$f_c(x_i, y_i) = N_c(x_i, y_i)/m \qquad (2)$$

$f_c(x_i, y_i)$: the fraction of class c of the (x_i, y_i) coarse pixel

$N_c(x_i, y_i)$: the number of fine pixels belonging to class c within the coarse pixel at (x_i, y_i)

m : the number of fine pixels within one coarse pixel

2) Estimating the temporal change of each class based on spectral linear mixing theory

The next step is calculating the temporal change of the pixel value in each class. According to spectral linear mixing theory, we could estimate the temporal change of a coarse pixel by weighting sum of the temporal change of all classes within it as follows:

$$\Delta C(x_i, y_i, b) = \sum_{c=1}^{l} f_c(x_i, y_i) \times \Delta F(c, b) \quad (3)$$

$$\Delta C(x_i, y_i, b) = C_2(x_i, y_i, b) - C_1(x_i, y_i, b) \quad (4)$$

b : band b

l : number of class

$\Delta C(x_i, y_i, b)$: change of band b value of the (x_i, y_i) coarse pixel between t_1 and t_2

$\Delta F(c, b)$: change of band b value of class c at fine resolution between t_1 and t_2

3) Predicting the fine resolution image and residuals from temporal changes

This step assumes as land cover types do not change between t_1 and t_2. Thus, the temporal change between t_1 and t_2 can be written as adding the temporal change to values of fine pixel at t_1:

$$F_2^{TP}(x_{ij}, y_{ij}, b) = F_1(x_{ij}, y_{ij}, b) + \Delta F(c, b) \quad (5)$$

$F_2^{TP}(x_{ij}, y_{ij}, b)$: temporal prediction

$F_1(x_{ij}, y_{ij}, b)$: band b value of the jth fine pixel within the coarse pixel at location (x_i, y_i) observed at t_1

The temporal prediction of fine resolution image at t_2 is not a very accurate prediction where land cover type change has occurred and the area has a large variability within-class. Therefore, in FSDAF there is a step estimating the residual between the true values and temporal prediction of fine pixels.

$$\frac{1}{m}\sum_{j=1}^{m} F_2(x_{ij}, y_{ij}, b) = \frac{1}{m}\sum_{j=1}^{m} F_2^{TP}(x_{ij}, y_{ij}, b) + R(x_i, y_i, b) \quad (6)$$

Each coarse pixel value is equal to the sum of the values of all the fine pixels within it and a bias factor ξ. Bias factor ξ is the system difference between two sensors caused by bandwidth and solar geometry difference (Gao et al. 2006). As system difference can be considered as a constant between t_1 and t_2, the values of coarse pixels at t_1 and t_2 can be written as follows:

$$C_1(x_i, y_i, b) = \frac{1}{m}\sum_{j=1}^{m} F_1(x_{ij}, y_{ij}, b) + \xi \quad (7)$$

$$C_2(x_i, y_i, b) = \frac{1}{m}\sum_{j=1}^{m} F_2(x_{ij}, y_{ij}, b) + \xi \quad (8)$$

From equation (7) to (9), we can derive the equation to obtain the residual $R(x_i, y_i, b)$:

$$R(x_i, y_i, b) = \Delta C(x_i, y_i, b) - \frac{1}{m}[\sum_{j=1}^{m} F_2^{TP}(x_{ij}, y_{ij}, b) - \sum_{j=1}^{m} F_1(x_{ij}, y_{ij}, b)] \quad (9)$$

4) Obtain TPS interpolation to predict the spatial variation of coarse image between t_1 and t_2

The change of the pixel value according to the temporal change of each class is considered, but the spatial change due to the land cover change is not considered. The FSDAF used the thin plate spline (TPS) method which is a spatial interpolation method for point data based on spatial dependence to downscale the coarse resolution image at t_2 for spatial prediction. Each

coarse pixel value is attributed to the center location to obtain a regular point data set. TPS first fits a spatial dependent function using the known point data through minimizing an energy function. The strength of TPS prediction is that it reflects the land cover type changes and local variabilities in the result between t_1 and t_2.

5) Residual distribution to fine pixels

Distributing residuals from temporal prediction to each of fine pixel within coarse pixel is the important step to improve the accuracy of temporal prediction. The FSDAF used a weighted function that distributes more residuals to the sub-pixels with larger errors.

Where the landscape is homogenous, TPS prediction presents true values of the fine pixel at t_2. The temporal prediction error can be estimated as follows:

$$E_{ho}(x_{ij}, y_{ij}, b) = F_2^{SP}(x_{ij}, y_{ij}, b) - F_2^{TP}(x_{ij}, y_{ij}, b) \qquad (10)$$

However, the error that is estimated is not valid for fine pixels where landscapes are heterogeneous or edges where more than two land cover types meet. This is because, TPS prediction makes these edges smooth. In heterogeneous landscapes, or at land cover edges, assuming that all fine pixels within coarse pixel get equal errors is reasonable as if there is no other information available to use:

$$E_{he}(x_{ij}, y_{ij}, b) = R(x_{ij}, y_{ij}, b) \tag{11}$$

To integrate the two cases into one weighted function to guide the residual distribution, the FSDAF used a homogeneity index as follows:

$$HI(x_{ij}, y_{ij}) = (\sum_{k=1}^{m} l_k)/m \tag{12}$$

Where l_k approaches to 1, it means that the kth fine pixels within a moving window with the same land cover type as the central fine pixel (x_i, y_i) is being considered, otherwise l_k approaches to 0. The value range of HI is between 0 and 1, closer to 1 indicates a homogeneous landscape, smaller values indicates a heterogeneous landscape. The weight for combining

the two cases through HI can be calculated as follows:

$$CW(x_{ij}, y_{ij}, b) = E_{ho}(x_{ij}, y_{ij}, b) \times HI(x_{ij}, y_{ij}, b) + E_{he}(x_{ij}, y_{ij}, b) \times (1 - HI(x_{ij}, y_{ij}, b)) \quad (13)$$

Then the weight is normalized as follows:

$$W(x_{ij}, y_{ij}, b) = CW(x_{ij}, y_{ij}, b) / \sum_{j=1}^{m} CW(x_{ij}, y_{ij}, b) \quad (14)$$

The residual is then distributed to the jth fine pixel as follows:

$$(x_{ij}, y_{ij}, b) = m \times R(x_i, y_i, b) \times W(x_{ij}, y_{ij}, b) \quad (15)$$

The FSDAF obtains the prediction of the total change by summing the temporal change and distributed residual of fine pixel between t_1 and t_2:

$$\Delta F(x_{ij}, y_{ij}, b) = R(x_i, y_i, b) + \Delta F(c, b) \quad (16)$$

6) Get a robust prediction of a fine image using neighborhood

Finally, to reduce the uncertainties in final predictions while

minimizing block effect, the FSDAF obtain a more robust prediction of fine pixel values at t_2. The FSDAF uses the weight that is determined by the spatial distance between the target pixel and similar pixel. By adding this final estimation of total change to the initial observation at t_1, the final prediction of the target pixel at t_2 can be calculated as follows:

$$F_2(x_{ij}, y_{ij}, b) = F_1(x_{ij}, y_{ij}, b) + \sum_{k=1}^{n} w_k \times \Delta F(x_k, y_k, b) \qquad (17)$$

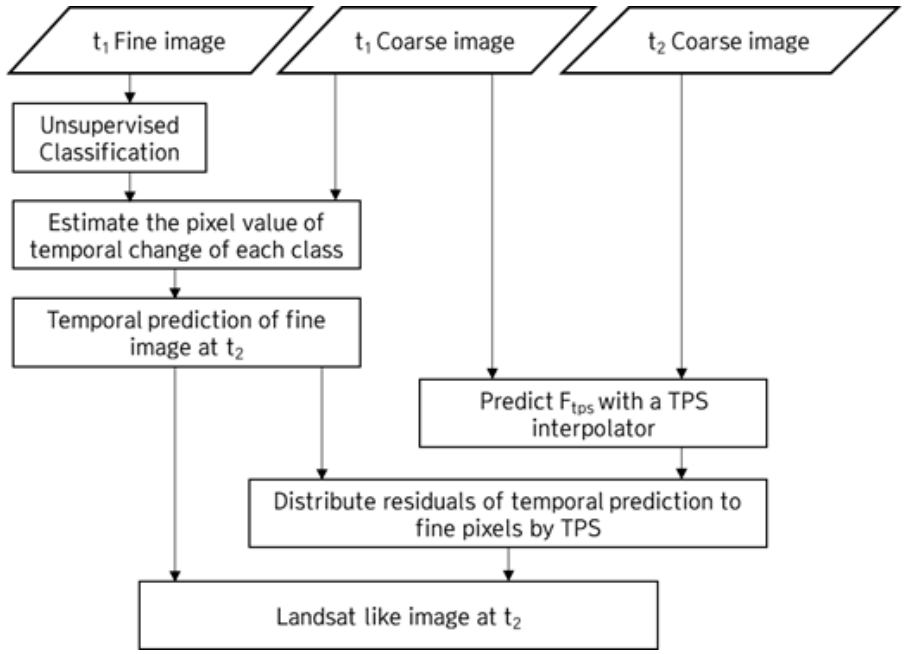

Figure 3. Flow chart of FSDAF fusion method (Remade flowchart based on Zhu et al. 2016)

3.2.3.2. Image fusion using RDSFM method

Previous image fusion techniques had limitations in predicting the spectral change area between the reference image and the predicted image. Although, FSDAF shows relatively high prediction accuracy with minimal input data in heterogeneous landscapes, but has a limitation when various land cover types exist in one coarse pixel. The same weight will be distributed to all bands so that especially in vegetation area the spectral change of each band could not be considered and this would result in critical error (Jin 2018). Therefore, we used RDSFM which solved these limitations to construct continuous image.

The RDSFM detects the degree of change of each band value through the correlation between the fine image at time t_1 and the coarse image at time t_2 using Iteratively Regularized Multivariate Alteration Detection (IR-MAD) technique, a non-supervised change detection technique. Applying the weight to the pixels where spectral change occurred between two images solves the limitations of the FSDAF which could not reflect the change of each band value. The RDSFM has five main steps as follows (Figure 4).

1) Estimate fine resolution image at t_2 using unmixing method

This step assumes that the temporal change of the coarse pixels is equal to the weighted sum of the temporal change of all classes within it. First, in order to calculate the fraction of each land cover type within the coarse pixel, we used unsupervised classification (ISO DATA) of Landsat image at t_1. Then the fraction of each class is calculated as follows:

$$f_c(x_i, y_i) = N_c(x_i, y_i)/m \quad (17)$$

$f_c(x_i, y_i)$: the fraction of class c of (x_i, y_i)

$N_c(x_i, y_i)$: the number of fine pixels belonging to class c within the coarse pixel at (x_i, y_i)

m : the number of fine pixels within one coarse pixel

The next step is calculating the fraction of each class in each coarse pixel and the temporal change of each class. According to the spectral linear mixing theory, we can assume the temporal change of the coarse pixels is equal to the weighted sum of the temporal change of all classes within it (see Equations 18-19). In this case, it is assumed that there is no land cover change

between t_1 and t_2.

$$\Delta C(x_i, y_i, b) = \sum_{c=1}^{l} f_c(x_i, y_i) \times \Delta F(c, b) \quad (18)$$

$$\Delta C(x_i, y_i, b) = C_2(x_i, y_i, b) - C_1(x_i, y_i, b) \quad (19)$$

b : band b

l : the number of classes

$\Delta C(x_i, y_i, b)$: change of band b value of the (x_i, y_i) coarse pixel between t_1 and t_2

$\Delta F(c, b)$: change of band b value of class c at fine resolution between t_1 and t_2

$C_1(x_i, y_i, b)$: band b value of coarse pixel at location (x_i, y_i) observed at t_1

$C_2(x_i, y_i, b)$: band b value of coarse pixel at location (x_i, y_i) observed at t_2

The fine image at time t_2 could be predicted using the changed value of each class of MODIS image. In this step, if the spatial change between t_1 and t_2 does not occur, the temporal change of the fine image at time t_2 could be predicted by adding the temporal change value to the fine pixel at the time t_1 as follows:

$$F_2^{TP}(x_{ij}, y_{ij}, b) = F_1(x_{ij}, y_{ij}, b) + \Delta F(c, b) \quad (20)$$

$F_2^{TP}(x_{ij}, y_{ij}, b)$: temporal prediction

$F_1(x_{ij}, y_{ij}, b)$: band b value of the jth fine pixel within the coarse pixel at location (x_i, y_i) observed at t_1

2) Predict fine resolution image and residuals from temporal image

There is a difference in the value between the changed value of the actual pixel and the predicted pixel, which is called the residual. The residuals are mainly caused by changes in spectral information due to land cover change of each class (Zhu et al. 2016). Distributing the residuals to the fine pixels within the coarse pixel is key process for the improvement of the prediction accuracy of the fine pixel at time t_2. The residual between the actual pixel and the predicted pixel can be calculated as follows:

$$R(x_i, y_i, b) = \Delta C(x_i, y_i, b) - \Delta F(x_i, y_i, b) \quad (21)$$

FSDAF distributes the residuals based on the degree of heterogeneity but depends on the class that is classified at the t_1. In other words, even though the land cover is different, the error may occur in some areas because the reflectance values could be similar at certain times.

3) Estimate MAD-based weights using IR-MAD method

The IR-MAD method is a representative non-supervised change detection technique which is usually applied to a 30m multispectral image such as Landsat because of its good performance (Nielsen 2007). The IR-MAD method is a simple iterative scheme which places high weights on observations where little change exhibited over time. IR-MAD method is based on canonical correlation analysis, tries to identify linear combination between the two variables, $a^T X$ and $b^T Y$, to maximize the objective function $max_{a,b} var(a^T X - b^T Y)$ with $\mathrm{V}\{a^T X\} = V\{b^T Y\} = 1$.

The dispersion matrix of the MAD variates is calculated as follows:

$$D = \mathrm{V}\{a^T X - b^T Y\} = V\{a^T X\} + V\{b^T Y\} - 2cov\{a^T X, b^T Y\} = 2(1 - \mathrm{corr}\{a^T X, b^T Y\}) \quad (22)$$

To distribute more appropriate residuals to each subpixel, we used the weight based on multivariate analysis between t_1 and t_2 images using IR-MAD method. It estimates the change of multivariate data of the same area. The MAD value derived from the IR-MAD method is a relative value, which represents 0 in the pixel where no change occurs or the absolute value where the significant change had occur.

The MAD variate can be expressed as the difference between the highest order canonical variates and it can be expressed as Equation (23).

$$\begin{bmatrix} X \\ Y \end{bmatrix} \rightarrow \begin{bmatrix} a_p^T X - b_p^T Y \\ \vdots \\ a_p^T X - b_p^T Y \end{bmatrix} \quad (23)$$

a_i, b_i : coefficient from a standard canonical correlation analysis

Through a brief derivation, the objective function can be reformulated to minimize the correlation between the two variables, $min\lambda = corr\ (a^TX,\ b^TY)$. The $corr$ represents the correlation function. The correlation can be formulated to Rayleigh quotients as we let the variance-covariance matrix of X and Y be Σ_{XX} and Σ_{YY}, respectively, and their covariance be Σ_{XY}.

$$\min\lambda^2 = \frac{a^T \sum_{XY} \sum_{YY}^{-1} \sum_{YX} a}{a^T \sum_{XX} a} = \frac{b^T \sum_{XY} \sum_{XX}^{-1} \sum_{YX} b}{b^T \sum_{XX} b} \qquad (24)$$

Equation (24) is an eigenvalue problem, which is $\sum_{XY} \sum_{YY}^{-1} \sum_{YX} a = \lambda^2 \sum_{XX} a$. The solutions are the eigenvectors of $a_1 \ldots\ldots a_n$ corresponding to the eigenvalues $\lambda_1^2 \geq \cdots \geq \lambda_n^2 \geq 0$ of $\sum_{XY} \sum_{YY}^{-1} \sum_{YX}$ with respect to Σ_{XX}. If we assume that the MODIS image is preprocessed to be zero mean, we can denote $\mathbf{MAD} = a^TX - b^TY$ as the MAD components of the combined bi-temporal image. Since the MAD variates is a linear combination of the measured variables, an approximate Gaussian distribution with the central limit theorem would be derived. Thus, MAD can represent the relative changes in subpixels in a coarse pixel. We

used IR-MAD ENVI extension made by Mort Canty (2013) to run IR-MAD and to derive the MAD variates. The MAD values are determined by the correlations between the two images at t_1 and t_2. The larger value means the spectrum changed a lot. The lower value means spectrum didn't change and the areas in the image are the same as the previous one. For the input of the IR-MAD method, a fine image at t_1 and a coarse image at t_2 were resampled through the bilinear interpolation method.

4) Residual distribution to the fine pixel

Errors of temporal prediction are mainly caused by changes of land cover and classes within the image. Therefore, we used a weighted function, considering the variates in each band and also the heterogeneous degree, to distribute the residuals to sub pixels. Multivariate-based weights can be calculated by Equation (25) as follows:

$$W_{MAD}(x_{ij}, y_{ij}, b) = MAD(x_{ij}, y_{ij}, b) / \sum_{i=1}^{m} MAD(x_{ij}, y_{ij}, b) \qquad (25)$$

Zhu et al. (2016) proposed a method of distributing residuals based on homogeneity index (HI), which indicates heterogeneity. In this study, HI was used to distribute residuals as well as FSDAF.

$$HI(x_{ij}, y_{ij}) = (\sum_{k=1}^{m} l_k)/m \tag{26}$$

As l_k approaches to 1 means that the kth fine pixel within a moving window with the same land cover type as the center fine pixel (x_{ij}, y_{ij}) is being considered. Otherwise l_k approaches to 0. The value range of HI is between 0 and 1, closer to 1 indicates a homogeneous landscape, and a smaller value indicates a heterogeneous landscape. MAD-based weights and HI-based weights can be expressed as Equation (27) and can be normalized by Equation (28).

$$\begin{aligned} W(x_{ij}, y_{ij}, b) = R(x_{ij}, y_{ij}, b) * \left(1 - HI(x_{ij}, y_{ij})\right) + \\ R(x_{ij}, y_{ij}, b) * W_{MAD}(x_{ij}, y_{ij}, b) \end{aligned} \tag{27}$$

$$W_{Normalized}(x_{ij}, y_{ij}, b) = W(x_{ij}, y_{ij}, b) / \sum_{j=1}^{m} W(x_{ij}, y_{ij}, b) \quad (28)$$

Then, the residuals are distributed to the jth fine pixel as follows:

$$r(x_{ij}, y_{ij}, b) = W_{Normalized}(x_{ij}, y_{ij}, b) * R(x_{ij}, y_{ij}, b) \quad (29)$$

Integrating the distributed residuals and the temporal change, we can predict the total changed value of the fine pixel between t_1 and t_2 as follows:

$$\Delta F(x_{ij}, y_{ij}, b) = r(x_{ij}, y_{ij}, b) + [F_2^{TP}(x_{ij}, y_{ij}, b) - F_1(x_{ij}, y_{ij}, b)] \quad (30)$$

5) Final prediction using the information of neighborhood

Theoretically, by adding the total changed value estimated through Equation (30) to the fine pixel value at time t_1, we can

obtain the fine image at time t_2. However, since the prediction is processed on a pixel-by-pixel basis, uncertainties caused by errors may occur during the previous steps and the noise within all input images. In addition, a block effect due to the residual in the coarse pixel can occur. In order to minimize the uncertainties and block effects, additional neighborhood information was used as FSDAF (Zhu et al. 2016). First, n fine pixels which are the same class and have the smallest spectral difference from the target fine pixel within its neighborhood are selected for a target pixel (x_{ij}, y_{ij}) in the fine image at t_1 (Equation (31)).

$$S_k = \sum_{b=1}^{B} \left[\frac{\left| F_1(x_k, y_k, b) - F_1(x_{ij}, y_{ij}, b) \right|}{F_1(x_{ij}, y_{ij}, b)} \right] \tag{31}$$

$$D_k = 1 + \sqrt{(x_k - x_{ij})^2 + (y_k - y_{ij})^2} / (\frac{w}{2}) \tag{32}$$

where w is the size of the moving window and neighborhood. The value of D_k is range from 1 to $1 + \sqrt{2}$. If the similar pixels are far enough to contribute less to the estimated target pixel, the weight for kth similar pixel can be calculated as:

$$w_k = (\frac{1}{D_k}) / \sum_{k=1}^{n} (\frac{1}{D_k}) \quad (33)$$

To obtain the total changed value of the target pixel, the changed value of all similar pixels is summed by weight. The final prediction of the target pixel at t_2 can be calculated as the Equation (34) by adding final estimated total change to a fine image at t_1.

$$F_2(x_{ij}, y_{ij}, b) = F_1(x_{ij}, y_{ij}, b) + \sum_{k=1}^{n} w_k \times \Delta F(x_{ij}, y_{ij}, b) \quad (34)$$

In this study, continuous NDVI images of 2015 with a spatial resolution of 30m was constructed from January to December using the RDSFM. Then we made the $NDVI_{max}$ image of 2015 that reflects the healthiest status of the vegetation.

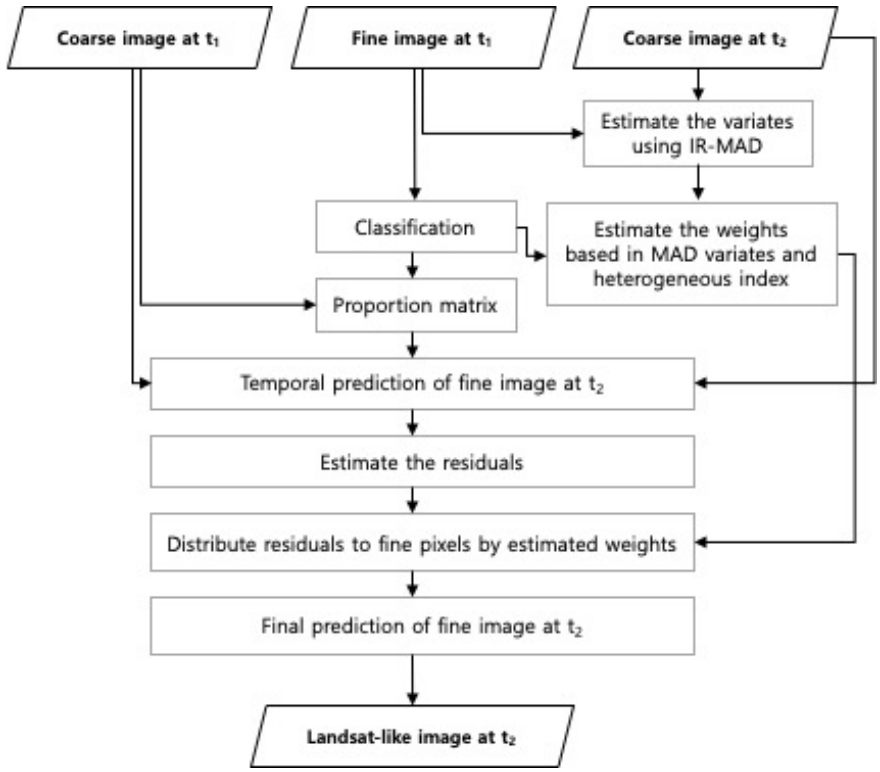

Figure 4. Flow chart of RDSFM fusion method (Remade flowchart based on Jin 2018)

3.2.4. Accuracy assessment of image fusion result

We verified the accuracy of the predicted image by comparing with the actual Landsat image using several indices. RMSE, R and AD were used for the accuracy verification. The RMSE was used to gauge the difference between the predicted image and the actual Landsat image reflectance value. The function of RMSE can be calculated as Equation (35). If the RMSE value is less than 0.1, we can say that the prediction accuracy of the predicted image is quite high (Chai & Draxler 2014).

$$RMSE = \sqrt{\frac{\sum_{i=1}^{n}(P_i - R_i)^2}{n}} \quad (35)$$

n : number of samples

P_i : predicted Landsat-like value of pixel i

R_i : actual Landsat value of pixel i

In order to analyze the linear relationship between the predicted Landsat-like image and the actual Landsat image, correlation coefficient R was calculated. If the correlation coefficient R is higher than 0.7, it is generally considered to have

a strong linear relationship (Lee & Noh 2013). The correlation coefficient R can be calculated using Equation (36).

$$R = \frac{\sum_{i=1}^{n}(x_i - \bar{x})(y_i - \bar{y})}{\sqrt{\sum_{i=1}^{n}(x_i - \bar{x})^2}\ \sqrt{\sum_{i=1}^{n}(y_i - \bar{y})^2}} \quad (36)$$

x_i : predicted Landsat-like value of pixel i

y_i : actual Landsat value of pixel i

$\bar{x} = \frac{1}{n}\sum_{i=1}^{n} x_i$

$\bar{y} = \frac{1}{n}\sum_{i=1}^{n} y_i$

The AD index was used to estimate the overall bias of prediction between the actual Landsat image and the Landsat-like predicted image. The positive AD value indicates that the pixel values of the predicted image are overestimated than the actual image pixel value and the negative AD value indicates that the pixel values of the predicted image are underestimated than the actual image pixel value.

The actual Landsat image with less than 2% cloud cover was used for the accuracy verification of the predicted Landsat-like

image. Table 2 shows the information of the March and September images, which have a relatively low cloud cover among the Landsat images of 2015. In addition, the prediction accuracy result of RDSFM was compared with FSDAF's, which represents a high accuracy prediction in heterogenous area, to test as if it is suitable to complicated landscape such as Seoul Metropolitan area.

3.2.5. Classification of adjacent land cover types and forest edge

This study used the classification method of Sung et al. (2018). The adjacent land cover type was selected from the land cover map (2013) provided by the EGIS (Environmental Geographic Information Service). We extracted the land cover type that were mainly neighbored by the forest edge by setting 30m buffer from Seoul urban forest (Figure 5). The adjacent land cover types that were mainly neighbored by the forest edge were residential area, road, agriculture area, grassland. We set 90m buffer from the mainly neighbored land covers to analyze the difference in vegetation condition due to adjacent land cover types. We also

set the 30m intervals to 90m buffer from the mainly neighbored land covers to the forest interior to estimate the distance that each land cover type affects (Figure 5).

We used the 5th forest type map provided by Korea Forest Service (KFS) to classify the urban forest edge to each forest types and 6 age classes. After overlapping each of buffer areas of mainly neighbored land cover type and urban forest edge areas that were classified, stratified sampling was conducted to compare $NDVI_{max}$ values of each type that we classified. However, the forest edges which were affected by various land cover types were excluded in this analysis to minimize multiple impact of adjacent land covers (Sung et al. 2018). As a result, only the forest edges of age class 4 were used in this analysis because the sampling points of other age classes were few. The stratified sampling and extraction of the overlapped areas were performed using ArcGIS 10.2.2.

Vegetation condition differences of forest edge which were neighbored by each land cover type and located in each 30m interval buffer were analyzed. The ANOVA analysis was conducted to detect the significant differences of $NDVI_{max}$ among

the adjacent land cover types and the distance using SPSS software.

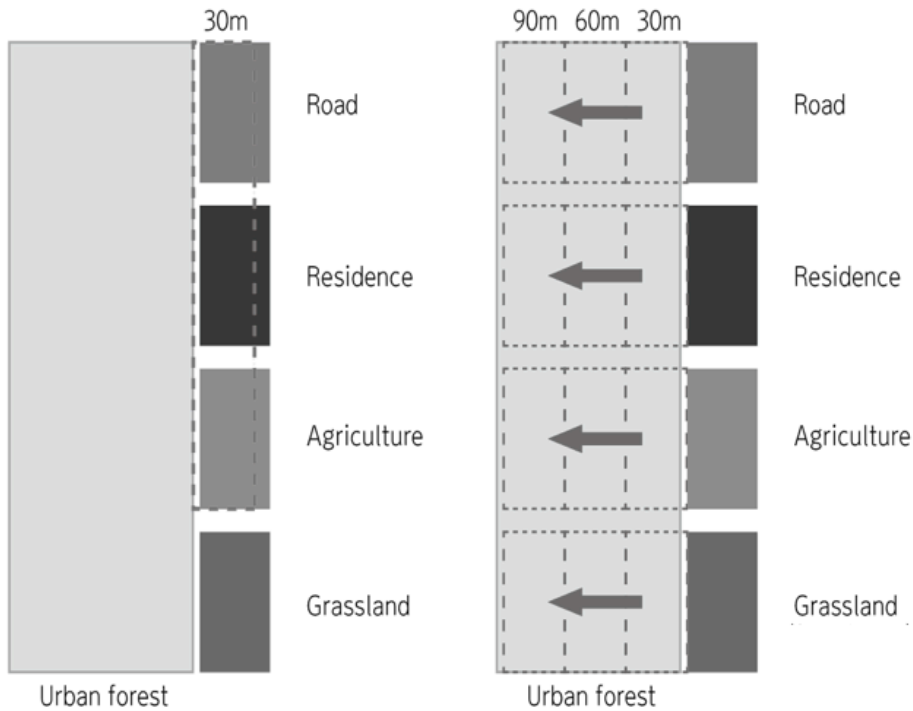

Figure 5. Classification of adjacent land cover types(left) and setting buffer distance from land cover types(right) (Sung et al. 2018)

Chapter 4. Results and Discussions

4.1. Image fusion and accuracy assessment results

$NDVI_{max}$ image derived from continuous NDVI images with spatial resolution of 30 m from January to December 2015 is presented in Figure 6. We can see that the urban forest of Seoul is well reflected in the derived image. Table 3 shows the results of the accuracy assessment by comparing the reflectance values of the Landsat-like predicted image derived by the RDSFM and the reflectance values of the actual Landsat image.

Table 4 shows the results of the accuracy assessment by comparing the reflectance values of the Landsat-like predicted image derived by the FSDAF and the reflectance values of the actual Landsat image. We can see the RMSE of red band (band3) and NIR band (band4), which are used for calculating NDVI image, on March and September are in the range 0.0199 ~ 0.0323. This means the reflectance values between predicted and actual image of March and September are quite similar. The correlation

coefficient R of red band (band3) and NIR band (band4) on March and September are in the range 0.8239~0.8620, which represents relatively high correlation between the reflectance values of predicted and actual image. The AD values of red band (band3) and NIR band (band4) on March and September reveal less than 0.03, indicating the overall bias of the predicted results is nearly unbiased.

Compared to FSDAF, RDSFM has a slight improvement in predicting the NIR band value and red band value. This is considered to be a result of weights according to the MAD, calculated from the correlation between the fine image at the time t_1 and the coarse image at the time t_2. In this study, we used RDSFM which shows a slightly better prediction accuracy than FSDAF. It is more suitable than FSDAF for forest edge studies in urban areas which have heterogeneous land covers like Seoul Metropolitan area.

Theoretically we could derive daily predicted image because the input data of RDSFM is daily MODIS images. However, it still has a low pixel quality during the rainy season or where it is regionally cloudy. Using higher temporal resolution image for

input data will be a solution for this limitation. Also using higher spatial resolution images would represent a better result in predicting images. Besides the image fusion techniques, CubeSat which provides high spatio-temporal resolution image, could be an alternative method to monitor land surface (Houborg & McCabe 2018).

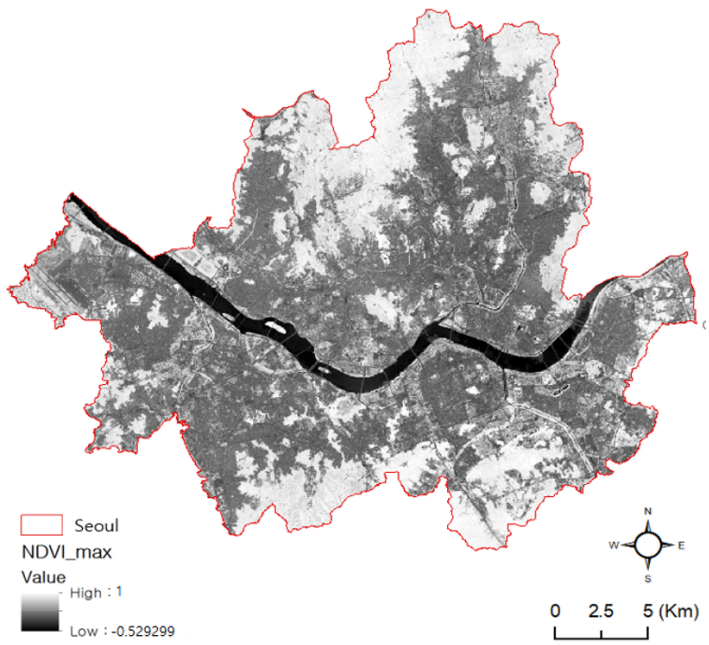

Figure 6. $NDVI_{max}$ image made by monthly fused NDVI image

Table 3. Accuracy assessment applied to march and September RDSFM fused image (band1: blue, band2: green, band3: red, band4: NIR, band5: SWIR1, band6: SWIR2)

	March			September		
	R	RMSE	AD	R	RMSE	AD
Band1	0.8134	0.0293	0.0051	0.8451	0.0324	0.0164
Band2	0.7790	0.0439	0.0220	0.9093	0.0420	0.0214
Band3	**0.8620**	**0.0199**	**0.0028**	**0.8239**	**0.0323**	**0.0225**
Band4	**0.8568**	**0.0228**	**0.0031**	**0.8305**	**0.0312**	**0.0192**
Band5	0.6524	0.1040	0.0883	0.8515	0.0333	0.0056
Band6	0.8358	0.0329	-0.0018	0.8800	0.0282	0.0018

Table 4. Accuracy assessment applied to march and September FSDAF fused image (band1: blue, band2: green, band3: red, band4: NIR, band5: SWIR1, band6: SWIR2)

	March			September		
	R	RMSE	AD	R	RMSE	AD
Band1	0.8060	0.0298	0.0052	0.8415	0.0326	0.0016
Band2	0.7642	0.0445	0.0219	0.9082	0.0422	0.0214
Band3	**0.8573**	**0.0202**	**0.0028**	**0.8169**	**0.0325**	**0.0222**
Band4	**0.8538**	**0.0230**	**0.0032**	**0.8265**	**0.0314**	**0.0190**
Band5	0.6543	0.1036	0.0882	0.8504	0.0333	0.0054
Band6	0.8238	0.0339	-0.0018	0.8765	0.0289	0.0016

4.2. Difference of forest edge vegetation index by land cover types

Assessing the impact of adjacent land cover is important for urban forest management (Alighier & Deconchat 2013). Therefore, we analyzed the differences of $NDVI_{max}$ of forest edges within the 90m buffer from the 4 land cover types. $NDVI_{max}$ of the forest edge was significantly different according to the adjacent land cover type with the F-value of 41.49 ($P < 0.05$) and 59.173 ($P < 0.05$) in both broad leaf and needle leaf forest edges, respectively (Table 5). The forest edge neighbored by road had the lowest $NDVI_{max}$ mean value of 0.818 and 0.805 in broadleaf forest edge and needle leaf forest edge, respectively (Table 5). This implies that the impact of roads on the forest edges is greater than other land covers, and has more influenced the environment such as microclimate and temperature (Delgado et al. 2007) of the forest edge. It is considered that these influences resulted in lower $NDVI_{max}$ mean value.

The $NDVI_{max}$ mean value of forest edge neighbored by agricultural area was higher than that of residential areas and

roads. It is considered that agricultural area can be used as a buffer zone to conserve vegetation from the developed area. In the case of grassland, $NDVI_{max}$ mean value was higher than that of the road, but lower than that of the residential area and agricultural area. These results are expected because we contained not only natural grassland but also grassland that were cut off area or construction area in the past.

Table 5. Difference in vegetation condition ($NDVI_{max}$) according to land cover types in forest edge

NDVI	Land cover	Vegetation type	Mean	Std.	F(sig.)
Max	Road	Broad leaf forest	0.818	0.132	41.493 (P=0.000)
	Residence		0.860	0.078	
	Agriculture		0.890	0.086	
	Grassland		0.861	0.133	
Max	Road	Needle leaf forest	0.805	0.091	59.173 (P=0.000)
	Residence		0.836	0.102	
	Agriculture		0.877	0.079	
	Grassland		0.838	0.116	

4.3. Difference of forest edge vegetation index by distance to interior forest

As a result of $NDVI_{max}$ mean values at 90m buffer (Table 5), it is hard to evaluate the distance affected by adjacent land cover more specifically. In addition, the pixels which is located in the 30m to 90m buffer are all included, the result of $NDVI_{max}$ mean values seem to be relatively high (Table 5). Therefore, we conducted an additional analysis by setting the 30m buffer intervals to 90m from the forest edge (Figure 7, Table 6).

Table 6 is the result of ANOVA analysis to detect the significant differences of $NDVI_{max}$ value according to distance from the forest edge. The difference in the $NDVI_{max}$ values between the forest edges were significantly different except needle leaf forest edge neighbored by the agricultural area. This is because most of the agricultural area were surrounded by the forest, so the neighbored forest edges were less affected by the distance than other land cover types.

Figure 7 is the result of the $NDVI_{max}$ mean values of forest edges at 30m, 60m, and 90m. It shows that the $NDVI_{max}$ mean values have an increasing trend toward the forest interior in both broad and needle leaf forest. We confirmed that the forest edges have a lower $NDVI_{max}$ mean values than the forest interiors.

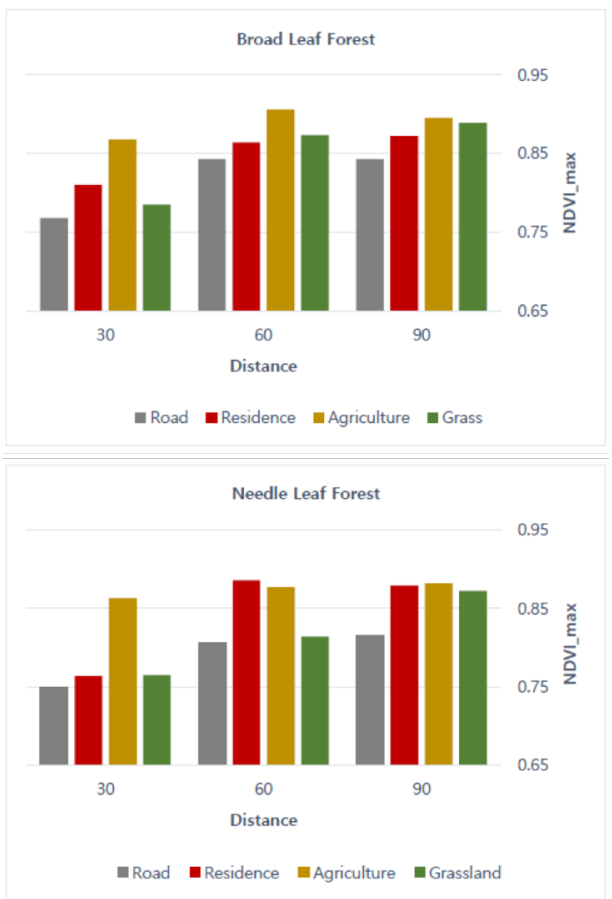

Figure 7. Difference in vegetation condition ($NDVI_{max}$) according to distance in broad leaf forest edge(up) and needle leaf forest edge(down)

As a result of distance analysis, it was found that the 0-30m forest edge were affected the most. Especially, the 0-30m forest edge neighbored by road showed the lowest $NDVI_{max}$ mean values among the land cover types. This means that the effects of roads have the greatest influence up to 30 m as the previous study that revealed greatest influence up to 20m from the road (Marcantonio et al. 2013). We also found that the $NDVI_{max}$ value up to 90 m from the road were lowest among the land cover types which means that the range of road impacts were wider than other land cover types. This means the management of the forest edges nearby roads will be necessary during road development or after development.

The $NDVI_{max}$ values neighbored by residential area tend to increase from the forest edge to the interior in both broad leaf and needle leaf forest, and the $NDVI_{max}$ value of 0-30m forest represented the lowest value. The $NDVI_{max}$ values of 0-30m forest edge neighbored by agricultural area had the lowest value as well, but higher $NDVI_{max}$ values than other land covers. This suggests that agricultural area seems to minimize the impacts from the development area and could be used to conserve the

forest which are neighbored by the developing site or the area after development.

In the case of grassland, the $NDVI_{max}$ value was found to be lowest on 0-30m forest edge as well and have an increasing trend with the distance to the forest interior. The $NDVI_{max}$ value of forest edges neighbored by grassland were relatively low. This result is expected because we contained not only the natural grassland area but also the area that were cut off or were a construction area in the past.

Table 6. Difference in vegetation condition ($NDVI_{max}$) according to distance from land cover types in forest edge

NDVI	LULC	Distance	Vegetation type	Mean	Std.	F(sig.)
Max	Road	30m	Broad leaf forest	0.768	0.150	22.08 (P=0.000)
		60m		0.843	0.118	
		90m		0.843	0.111	
Max	Road	30m	Needle leaf forest	0.750	0.133	6.078 (P=0.000)
		60m		0.807	0.122	
		90m		0.815	0.059	
Max	Residence	30m	Broad leaf forest	0.810	0.110	8.378 (P=0.000)
		60m		0.864	0.067	
		90m		0.872	0.068	
Max	Residence	30m	Needle leaf forest	0.764	0.105	41.875 (P=0.000)
		60m		0.886	0.050	
		90m		0.879	0.080	
Max	Agriculture	30m	Broad leaf forest	0.868	0.116	8.450 (P=0.000)
		60m		0.906	0.061	
		90m		0.895	0.067	
Max	Agriculture	30m	Needle leaf forest	0.863	0.107	1.223 (P=0.297)
		60m		0.877	0.074	
		90m		0.882	0.073	
Max	Grassland	30m	Broad leaf forest	0.785	0.188	13.656 (P=0.000)
		60m		0.873	0.119	
		90m		0.889	0.090	
Max	Grassland	30m	Needle leaf forest	0.765	0.153	13.921 (P=0.000)
		60m		0.814	0.141	
		90m		0.872	0.069	

Chapter 5. Conclusion

In this study, a continuous NDVI image was constructed using RDSFM. As the RDSFM distributes the MAD weight-based residuals to each band, it revealed slightly improved prediction accuracy compared to FSDAF. The $NDVI_{max}$ image of 2015 were derived based on continuous NDVI images constructed by the RDSFM. In this study, we used the $NDVI_{max}$ image to analyze the differences of vegetation condition and the distance that the forest edges are affected due to adjacent land cover types in Seoul Metropolitan area.

As a result of the vegetation condition difference in urban forest edges according to the adjacent land cover types based on the $NDVI_{max}$ images, it had a significant difference according to land cover types. Among the land cover types, which had the greatest effect on the forest edge was shown as road, and the effect range was found to be up to 90 meters from the forest edges. This means the management of the forest edges nearby roads will be necessary during road development or after development. The $NDVI_{max}$ value was the lowest in 0-30m forest

edge which were the most affected area, but had an increasing trend as the distance increased to forest interior in most of the land cover types.

However, in this study, there are limitations that we didn't consider road width, height of the building, albedo of the land covers that could be result in the difference of $NDVI_{max}$ values. In addition, we only used the $NDVI_{max}$ values to analyze the vegetation condition of the forest edges and didn't considered temperature, precipitation, and microclimate during the vegetation growth period.

This study is meaningful for evaluating the vegetation condition by different land cover types and comparing the vegetation condition from the edges to forest interiors by setting 30m intervals to 90m based on the images made by RDSFM. The results of this study are expected to be useful for evaluating the effects of land cover type and land cover change on adjacent forests in terms of urban forest monitoring and management.

The RDSFM used in this study is a pixel-based fusion technique that can be used with other resolution images not only

Landsat and MODIS images. In future studies, it will be possible to provide a better data for vegetation related studies using higher resolution inputs. Image fusion is a useful method to solve the problem where it is difficult to obtain continuous images with high spatial resolution due to the influence of clouds or it have difficulties to obtain images at desired date. Especially, the RDSFM could solve this limitation and have a high accuracy of prediction as well. It is considered to be widely applicable in various studies such as forest monitoring, forest deforestation, forest disturbance, vegetation phenology.

Besides the image fusion techniques CubeSat is also an alternative method to monitor land surface (Houborg & McCabe 2018). CubeSat has an advantage of high spatial resolution (3-5m) with low cost, but requires specific algorithm before using image so that it could have much more error by the researcher than the existing preprocessed satellite image. If further studies discuss more about current limitations of CubeSat, it would be possible to analyze more accurately than the predicted images and it will be applied to various study fields including vegetation studies.

Considering more specific data such as the change of more detailed vegetation communities and land cover types, the road construction completion date and the change of vegetation structure would be necessary to obtain better results and more meaningful results.

Bibliography

Akamphon, S., & Akamphon, K. (2014). Cost and benefit tradeoffs in using a shade tree for residential building energy saving. *The international journal published by the Thai Society of Higher Education Institutes on Environment*, *7*, 19-24

Alignier, A., & Deconchat, M. (2013). Patterns of forest vegetation responses to edge effect as revealed by a continuous approach. *Annals of Forest Science*, *70(6)*, 601-609

Baker, T.P., Jordan, G.J., Steel, E.A., Fountain-Jones, N.M., Wardlaw, T.J., & Baker, S.C. (2014). Microclimate through space and time: micro climatic variation at the edge of regeneration forests over daily, yearly and decadal time scales. *Forest Ecology and Management*, *334*, 174-184

Baldi, G., Nosetto, M.D., Aragón, R., Aversa, F., Paruelo, J.M., & Jobbágy, E.G. (2008). Long-term satellite NDVI data sets: Evaluating their ability to detect ecosystem functional changes in South America. *Sensors*, *8*, 5397-5425

Briber, B.M., Hutyra, L.R., Reinmann, A.B., Raciti, S.M., Dearborn, V.K., Holden, C.E., & Dunn, A.L. (2015). Tree productivity enhanced with conversion from forest to urban land covers. *Plos One*, *10*, e0136237

Chai, T., & Draxler, R.R. (2014). Root mean square error (RMSE) or mean absolute error (MAE) Arguments against avoiding RMSE in the literature. *Geoscientific Model Development, 7(3)*, 1247-1250

Chaplin-Kramer, R., Ramler, I., Sharp, R., Haddad, N.M., Gerber, J.S., West, P.C., Mandle, L., Engstrom, P., Baccini, A., Sim, S., Mueller, C., & King, H. (2015). Degradation in carbon stocks near tropical forest edges. *Nature Communications, 6*, 1-6

Cho, J. (2015). Unsupervised Change Detection for Very High-spatial Resolution Satellite Imagery by Using Object-based IR-MAD Algorithm. *Journal of the Korean Society of Surveying, Geodesy, Photogrammetry and Cartography, 33(4),* 297-304

Davies-Colley, R.J., Payne, G.W., & van Elswijk, M. (2000).

Microclimate gradients across a forest edge. *New Zealand Journal of Ecology, 24(2),* 111-121

Delgado, J.D., Arroyo, N.L., Arévalo, J.R., & Fernández-Palacios, J.M. (2007). Edge effects of roads on temperature, light, canopy cover, and canopy height in laurel and pine forests (Tenerife, Canary Islands). *Landscape and Urban Planning, 81*, 328-340

Emelyanova, I.V., McVicar, T.R., Van Niel, T.G., Li, L.T., & van Dijk, A.I.J.M. (2013). Assessing the accuracy of blending Landsat-MODIS surface reflectances in two landscapes with contrasting sptial and temporal dynamics: A framework for algorithm selection. *Remote Sensing of Environment, 133*,193-209

Escobedo, F.J., & Nowak, D.J. (2009). Spatial heterogeneity and air pollution removal by an urban forest. *Landscape and Urban Planning. 90,* 102-110

FLAASH, M. (2009). Atmospheric Correction Module: QUAC and FLAASH User's Guide, Version 4.7, Boulder, CO, USA

Gevaert, C.M., & García-Haro, F.J. (2015). A comparison of STARFM and an unmixing-based algorithm for Landsat and MODIS data fusion. *Remote Sensing of Environment, 156,* 34-44

Gobster, P.H., Westphal, L.M. (2004). The human dimensions of urban greenways: Planning for recreation and related experiences. *Landscape and Urban Planning, 68,*147-165

Gulci, S., Akay, A.E., Oguz, H., & Gulci, N. (2017). Assessment of the Road Impacts on Coniferous Species Within the Road-Effect Zone Using NDVI Analysis Approach. *Fresenius Environmental Bulletin, 26,* 1654-1662

Haddad, N.M., Brudvig, L.A., Clobert, J., Davies, K.F., Gonzalez, A., Holt, R.D., Lovejoy, T.E., Sexton, J.O., Austin, M.P., Collins, C.D., Cook, W.M., Damschen, E.I., Ewers, R.M., Foster, R.M., Jenkins, C.N., King, A.J., Laurance, W.F., Levey, D.J., Margules, C.R., Melbourne, B.A., Nicholls, A.O., Orrock, J.L., Song, D., & Townshend, J.R. (2015). Habitat fragmentation and its lasting impact on Earth's ecosystems. *Science Advances*, *1*, e1500052-e1500052.

Hansen, M.C., Potapov, P.V., Moore, R., Hancher, M., Turubanova, S.A., Tyukavina, A., Thau, D., Stehman, S.V., Goetz, S.J., Loveland, T.R., Kommareddy, A., Egorov, A., Chini, L., Justice, C.O. & Townshend, J.R.G. (2013). High-Resolution Global Maps of 21st

Century forest cover change. *Science, 342*, 850-854.

Harper, K.A., Macdonald, S.E., Burton, P.J., Chen, J., Brosofske, K.D., Saunders, S.C., & Esseen, P.A. (2005). Edge Influence on Forest Structure and Composition in Fragmented Landscapes. *Conservation Biology, 19(3),* 768-782

Hernandez-Santana, V., Asbjornsen, H., Sauer, T., Isenhart, T., Schilling, K., & Schultz, R. (2011). Enhanced transpiration by riparian buffer trees in response to advection in a humid temperate agricultural landscape. *Forest Ecology and Management*, *261*, 1415-1427

Hofmeister, J., Hošek, J., Brabec, M., Hédl, R., & Modrý, M. (2013). Strong influence of long-distance edge effect on herb-layer vegetation in forest fragments in an agricultural landscape. *Perspective in Plant Ecology Evolution and Systematics,* 15, 293-303

Houborg, R., & McCabe, M.F., (2018). A CubeSat enabled Spatio-Temporal Enhancement Method (CESTEM) utilizing Planet, Landsat and MODIS data. *Remote Sensing Environment, 209,* 211-226

Jin, Y.H., Zhu, J.R., Sung, S.Y., & Lee, D.K. (2017). Impact assessment of forest development on Net Primary Production using satellite image spatial-temporal fusion and CASA-Model. *The Korea Society of Environmental Restoration Technology, 20(4),* 29-42

Jin, Y.H. (2018). Classification of Deforested and Degraded Areas in North Korea Using Phenology-based Indices and Spatiotemporal Data Fusion Method. PH.D. dissertation. Seoul National University, Seoul.

Khosravi, H., Haydari, E., Shekoohizadegan, S., & Zareie, S. (2017). Assessment the Effect of Drought on Vegetation in Desert Area using Landsat Data. *Egyptian Journal of Remote Sensing and Space Science, 20*, S3-S12

Kim, E.Y., Song, W.K., Yoon, E.J., & Jung, H.J. (2016). Definition of Invasive Disturbance Species and its Influence Factor: *Review. Journal of the Korea Society of Environmental Restoration Technology, 19(1)*, 155-170

Kim, E.Y., Wie, G.J., Cho, H.M., & Yang, I.T. (2010). A study for Forest Research using Airborne Laser Scanning. *Journal of the Korean Society of Surveying, Geodesy, Photogrammetry and*

Cartography, *28(3),* 299-304

Kim, S.H., & Jang, D.H. (2014). Analysis of forest types and estimation of the forest carbon stocks using landsat satellite images in Chungcheongnam-do, South Korea. *Journal of The Korean Association of Regional Geographers, 20(2),* 206-216

Kim, J.Y., & Jang, D.H. (2015). An application of remote sensing data for the land surface characteristics analysis of ecological stream restoration area in Daejeon stream. *Journal of the Association of Korean Geographers, 4(2),* 231-240

Kuttler, W. (2008). The Urban Climate: Basic and Applied Aspects. In: Marzluff, J.M., Shulenberger, E., Endlicher, W., Alberti, M., Bradley, G., Ryan, C., ZumBrunnen, C, & Simon, U. *Urban Ecology*. Springer, 233-248

Lal, R. (2005), Forest Soils and Carbon Sequestration. *Forest Ecology and Management, 220(1-3),* 242 258

Lee, H., & Noh, S. (2013). Advanced Statistical Analysis: Theory and Practice. Moonwoosa Publishing.

Li, F., Song, G., Liujun, Z., Yanan, Z., & Di, L. (2017). Urban vegetation phenology analysis using high spatio-temporal NDVI time series. *Urban Forestry & Urban Greening, 25,* 43-57

Liu, D., & Zhu, X. (2012). An enhanced physical method for downscaling thermal infrared radiance. *IEEE Geoscience and Remote Sensing Letters, 9(4),* 690-694

Lowe, D. (2004), Distinctive image features from scale in variant keypoints. *International Journal of Computer Vision,* pp. 1-28

MacLean, M.G. (2017). Edge influence detection using aerial LiDAR in Northeastern US deciduous forests. *Ecological Indicators, 72,* 310-314

Magnago, L.F.S., Edwards, D.P., Edwards, F.A., Magrach, A., Martins, S.V., & Laurance, W.F. (2014). Functional attributes change but functional richness is unchanged after fragmentation of Brazilian Atlantic forests. *Journal of Ecology, 102,* 475-485

Magnago, L.F.S., Magrach, A., Barlow, J., Schaefer, C.E.G.R., Laurance, W.F., Martins, S.V., & Edwards, D.P. (2017). Do fragment size and edge effects predict carbon stocks in trees and lianas in tropical forests?. *Functional Ecology, 31,* 542-552

Maltamo, M., Packalen, P., Yu, X., Eerikainen, K., Hyyppa, J. & Pitkanen, J., (2005). Identifying and quantifying structural characters characteristics of heterogeneous boreal forests using laser scanner data. *Forest ecology and management, 216,* 41-50

Marcantonio, M., Rocchini, D., Geri, F., & Bacaro, G. (2013). Biodiversity , Roads and Landscape Fragmentation : Two Mediterranean Cases. *Applied Geography, 42*, 63-72

Markon, B.C.J. (2001). Survey USG. Seven year phenological record of Alaskan ecoregions derived from Advanced Very High Resolution Radiometer normalized difference vegetation index data. Open-File Report 01-11 U.S. Department of the Interior

Nielsen, A.A. (2007). The regularized iteraitvely reweighted MAD method for change detection in Multi-and Hyperspectral data. *IEEE Transactions on Image Processing*, *16*, 463-478

Numata, I., Cochrane, M.A., Souza Jr, C.M., & Sales, M.H. (2011). Carbon emissions from deforestation and forest fragmentation in the Brazilian Amazon. *Environmental Research Letters, 6,* 44003

Riedel, S.M., Epstein, H.E. (2005). Edge effects on vegetation and soils in a Virginia old-field. *Plant and Soil, 270,* 13-22

Riutta, T., Slade, E.M., Morecroft, M.D., Bebber, D.P., & Malhi, Y. (2014). Living on the edge: quantifying the structure of a fragmented vforest landscape in England. *Landscape Ecology, 29,* 949-961

Sentinel Hub [Internet]. Laboratory for geographical information systems, Ltd. [cited 2017 Nov 20]. Available from: https://www.sentinel-hub.com/max_service

Shahidan, M.F., Shariff, M.K.M., Jones, P., Salleh, E., & Abdul-lah, A.M. (2010). A comparison of Mesua ferrea L. and Hura crepitans L. for shade creation and radiation modification in improving thermal comfort. *Landscape and Urban Planning, 97,* 168-181

Shojanoori. R, & Shafri, H.Z.M. (2017). Review on the use of remote sensing for urban forest monitoring Review on the Use of Remote Sensing for Urban Forest Monitoring. *Arboriculture & urban forestry, 42(6),* 400-417

Snavely, N., Seitz, S.N., & Szeliski, R. (2006), Photo tourism: exploring

image collections in 3D. *ACM Transaction on Gtaphics, NewYork,* pp. 1-12

Sung, H.Y., & Park, O.J., (2000). A study on distribution and change of NDVI with land-cover change in city of Sungnam. *The journal of GIS Association of Korea, 8(2),* 275-288

Sung, S.Y., Lee, D.K., & Mo, Y.W. (2015). Comparison of Carbon Stock Between Forest Edge and Core by Using Connectivity Analysis. *Korean Society of Rural Planning, 21(4),* 27-33

Sung, W.G., Lee, D.K., & Jin, Y.H. (2018). Analyzing Difference of Urban Forest Edge Vegetation Condition by Land Cover Types Using Spatio-temporal Data Fusion Method. *Journal of Environmental Impact Assessment*, *27(3),* 279-290

Wales, B.A. (1972). Vegetation analysis of north and south edges in a mature oak-hickory forest. *Ecological Monographs, 42(4),* 451-471

Weng, Q., Fu, P., & Gao, F. (2014). Generating daily land surface temperature at Landsat resolution by fusing Landsat and MODIS data. *Remote Sensing of Environment, 145,* 55-67

White, J.C., Coops, N.C., Wulder, M.A., Vastaranta, M., Hilker, T., & Tompalski, P. (2016). Remote Sensing Technologies for Enhancing Forest Inventories: A Review. *Canadian Journal of Remote Sensing*, *42,* 619-641

Wu, M., Huang, W., Niu, Z., & Wang, C. (2015). Generating Daily Synthetic Landsat Imagery by Combining Landsat and MODIS Data. *Sensors, 15,* 24002-24025.

Wu, M., Wu, C., Huang, W., Niu, Z., Wang, C., Li, W., Hao, P. (2016). An improved high spatial and temporal data fusion approach for combining Landsat and MODIS data to generate daily synthetic Landsat imagery. *Information Fusion, 31,* 14-25

Wulder, M.A., Bater, C.W., Coops, N.C., Hilker, T., & White, J.C. (2008). The role of LiDAR in sustainable forest management. *The Forestry Chronicle, 84*

Xun, B., Yu, D., Liu, Y., Hao, R., & Sun, Y.. (2014). Quantifying isolation effect of urban growth on key ecological areas. *Ecological Engineering, 69,* 46-54

Zhu, X., Chen, J., Gao, F., Chen, X., & Masek, J.G. (2010). An enhanced

spatial and temporal adaptive reflectance fusion model for complex heterogeneous regions. *Remote Sensing of Environment, 114(11),* 2610-2623

Zhu, X., Helmer, E.H., Gao, F., Liu, D., Chen, J., & Lefsky, M.A. (2016). A flexible spatiotemporal method for fusing satellite images with different resolutions. *Remote Sensing of Environment, 172,* 165-177

Abstract (Korean)

개발 및 도시화, 인간의 영향으로 도심 내 산림 파편화 진행되고 산림 임연부가 증가함에 따라 도시 산림 관리 측면에서 도시 산림 임연부의 현황 파악과 모니터링의 중요성이 대두되고 있다. 도시 산림 임연부에 대한 모니터링에는 연구 규모상 정밀한 공간해상도와 높은 시간해상도가 요구된다. 현재 제공되고 있는 위성영상 중 접근성이 좋고 무료로 제공되는 Landsat이나 MODIS 영상은 각각 시간해상도와 공간해상도의 한계가 존재한다. 따라서 본 연구에서는 도시 산림 임연부의 현황 파악을 위해 시간적 예측, 공간적 예측에서 정확도가 높은 RDSFM(Residual Distribution based Spatio-temporal data Fusion Method) 영상 융합 기법을 활용하여 연속적인 NDVI 영상을 도출하고, 도출한 연속적인 NDVI 영상으로 $NDVI_{max}$ 영상을 구축하여 인접한 토지피복 유형에 따른 도시 산림 임연부의 식생활력도 차이와 산림 임연부에서 산림 내부로의 거리에 따른 식생활력도 차이를 비교하고 평가하는데 목적이 있다. 서울시 내 도로, 주거지, 농경지, 초지에 인접한 도시 산림 임연부를 대상으로 분석해 본 결과, 산림 내부로 갈수록 $NDVI_{max}$ 값이 증가하는 경향이 나타났다. 임연부에 인접한 4가지 토지피복 유형 중 도로가 산림 임연부에 미치는 영향이 가장 큰 것으로 나타났다. 특히, 도로로부터 산림 임연부의 30m 까지 그 영향이 가장 두드러지게 나타났으며, 90m까지 영향을 미치는 것으로 나타났다. 농경지의 경우, 주거지역과 도로와 같은 개발지에 인접한 산림에 비해 활엽수림과 침엽수림 모두에서 높은 $NDVI_{max}$ 값을 갖는 것으로 나타나 농경지를 개발지로부터 식생을 보존하는 완충지대로 이용할 수 있을 것으로 사료된다. 초지의 경우, 도로에 인접한 산림에 비해 높은 $NDVI_{max}$ 값을 나타냈으나, 주거지역과 농경지에 인접한 산림에 비해 낮은 $NDVI_{max}$ 값을 갖는 것으로 나타났다. 이는 자연초

지에 인접한 산림 뿐만 아니라 도로의 절토 부문 및 공사 지역의 사면을 초지로 조성한 기타초지에 인접한 산림도 포함하여 분석을 진행하여 상대적으로 낮은 값을 나타낸 것으로 사료된다. 본 연구는 기존 시공간 융합기법에 비해 개선된 RDSFM 융합기법을 활용하여 구축한 $NDVI_{max}$ 영상을 토대로 토지피복 유형에 따른 인접 산림의 식생활력도 및 산림 내부로의 거리에 따른 식생활력도를 비교하고 평가하였다는 점에서 의의가 있으며, 본 연구의 결과는 도시 산림 모니터링 및 도시 산림 임연부 관리 측면에서 토지피복 유형과 토지피복 변화가 인접한 산림에 미치는 영향을 평가하는데 기초자료로 활용 가능할 것으로 기대된다.

키워드 : 도시 산림, 산림 가장자리, 토지피복유형, 영상 융합, 정규식생지수

학번 : 2017-20179